

# Two-Qubit Module Based on Phonon-Coupled Ge Hole-Spin Qubits: Design, Fabrication, and Readout at 1–4 K

D.-M. Mei,<sup>1</sup> S. A. Panamaldeniya,<sup>1</sup> K.-M. Dong,<sup>1</sup> S. Bhattacharai,<sup>1</sup> and A. Prem<sup>1</sup>

<sup>1</sup>*Department of Physics, University of South Dakota, Vermillion, SD 57069, USA*

(Dated: January 6, 2026)

We present a device-level design for a two-qubit module based on phonon-coupled germanium (Ge) hole-spin qubits operating at 1–4 K. Building on prior work on phonon-engineered Ge qubits and phononic-crystal (PnC) cavities, we specify a lithography-ready layout that integrates two gate-defined hole-spin qubits in a strained Ge quantum well with a GHz PnC defect mode that mediates a coherent phonon-based interaction. We detail the SiGe/Ge heterostructure, PnC cavity design, and a compatible nanofabrication process flow, including the gate stack, membrane patterning and release, and RF/DC wiring. We further develop a readout architecture combining spin-to-charge conversion with RF reflectometry on a proximal charge sensor, supported by a cryogenic RF chain optimized for operation at 1–4 K. Finally, we outline the cryogenic measurement environment, tuning procedures, and a stepwise benchmarking program targeting single-qubit control, phonon-bandgap suppression of relaxation channels, and resolvable phonon-mediated two-qubit coupling. The resulting module provides a scalable template for medium-range coupling of Ge hole-spin qubits and connects materials and phonon engineering with circuit-level readout, enabling future experimental demonstrations of entangling gates, Bell-state generation, and phonon-enabled quantum sensing.

## I. INTRODUCTION

High-purity germanium (Ge) integrated with phononic-crystal (PnC) cavities has emerged as a promising platform for warm-operating quantum hardware, combining strong spin-orbit coupling, mature materials control, and engineered phonon environments. Over the past decade, strained Ge/SiGe heterostructures have enabled gate-defined hole-spin qubits with long coherence times, fast all-electrical control, and multi-qubit operation, establishing Ge as a leading CMOS-compatible qubit material alongside Si and III-V systems. [1–3] In parallel, quantum-acoustics experiments have shown that GHz phononic modes in nanostructured resonators can reach the quantum regime and serve as coherent buses or memories when coupled to microwave or solid-state qubits. [4–6] Together, these advances motivate architectures in which Ge hole spins interact with engineered phononic bandgaps and defect modes to suppress decoherence and mediate entangling interactions.

Building on this foundation, Mei *et al.* proposed a phonon-coupled Ge hole-spin architecture in which qubits are hosted in a strained Ge quantum well and coupled to localized PnC defect modes in a suspended Ge membrane. [7] Modeling in that work indicated that such devices can, in principle, support fast electric-dipole spin resonance (EDSR), phonon-bandgap protection of  $T_1$  and  $T_2^*$ , and medium-range phonon-mediated two-qubit gates at temperatures in the 1–4 K range—accessible with  $^4\text{He}$  or pulse-tube cryostats rather than dilution refrigerators. In related work, the GeQuLEP concept explores Ge-based quantum phononic spectroscopy as a route to detect sub-MeV dark matter using long-lived, high- $Q$  phonon excitations in high-purity Ge, further highlighting the utility of engineered Ge phononics for ultra-low-

threshold sensing. [8] Taken together, these studies identify a common opportunity: leveraging Ge phononics to realize warm-operating quantum devices that naturally interface with both quantum information processing and quantum sensing.

Beyond single- and few-qubit demonstrators, Ge hole-spin qubits provide a natural route toward scalable processors and networked architectures. Group-IV compatibility, isotopic purification, and CMOS-friendly processing enable dense quantum-dot arrays and multi-qubit modules with all-electrical control, as demonstrated in Si/Ge platforms with fast, high-fidelity two-qubit gates. [3, 9] Coupling Ge spin qubits to on-chip microwave or phononic resonators further supports modular designs in which local registers are linked by bosonic buses or interfaced to photonic channels for long-distance entanglement distribution and quantum networking. [6, 10, 11] In this context, a phonon-engineered Ge hole-spin platform operating at 1–4 K can function as both a high-coherence memory and a locally programmable processor while remaining compatible with emerging quantum-network blueprints based on distributed, cavity- or waveguide-coupled nodes.

Motivated by these advances, the present work is organized around a set of concrete, experimentally testable research questions that go beyond proof-of-principle single-qubit demonstrations. First, can PnC bandgaps engineered in a suspended Ge membrane suppress phonon-induced relaxation and preserve spin lifetimes  $T_1$  at elevated cryogenic temperatures (1–4 K)? Second, can a single localized phononic defect mode provide sufficiently strong and coherent spin-phonon coupling to mediate resolvable two-qubit interactions between spatially separated Ge hole-spin qubits? Third, can high-fidelity readout and control be achieved using radio-frequency charge sensing and cryogenic amplification without reliance on dilution refrigeration? Addressing these questions estab-

lishes whether phonon-engineered Ge hole-spin devices can serve as a scalable, warm-operating quantum hardware platform.

In this work we move from architecture to implementation by developing a complete, fabrication-ready design for a two-qubit module that can serve as a building block for larger Ge-based quantum processors and quantum sensors. The module consists of two gate-defined hole-spin qubits formed in a strained Ge quantum well, separated by approximately 50 nm and coupled through a localized PnC defect mode in a suspended Ge membrane. We analyze the heterostructure stack, electrostatic layout, and phononic design needed to realize strong spin-phonon coupling while maintaining high  $g$ -factor tunability and robust charge stability. Particular attention is given to fabrication choices compatible with established Ge growth and processing flows, including etch chemistries, membrane thickness, and metallization schemes. The results presented here constitute a complete device-level design and experimental roadmap; experimental realization and data will be reported in follow-up work.

This work constitutes the first integrated, fabrication-ready design of a two-qubit module in which PnC cavities are co-engineered with gate-defined Ge hole-spin qubits, complete with a compatible nanofabrication process flow, cryogenic readout architecture, and experimentally actionable performance benchmarks at 1–4 K.

The remainder of this paper is organized as follows. Section II introduces the overall two-qubit device concept and electrostatic layout, while Sec. III specifies the SiGe/Ge heterostructure and materials stack that support the phononic-crystal-integrated module. In Sec. IV we outline a compatible nanofabrication process flow, including mesa definition, gate patterning, membrane release, and RF/DC wiring. Section V presents the spin-to-charge conversion protocols, charge-sensor design, and RF signal chain for high-fidelity qubit readout, and Sec. VI details the cryogenic measurement environment for operation at 1–4 K. In Sec. VII we propose an experimental program with target metrics for single- and two-qubit control and for validating the engineered phononic environment. Section VIII discusses anticipated performance, extensions of the architecture, and broader implications for scalable Ge-based quantum processors and quantum sensors. Finally, Sec. IX summarizes the main design outcomes and highlights paths toward multi-qubit scaling and integration into larger quantum-network architectures. Compared with our earlier work in Ref. [7], which focused on single-qubit modeling and parameter optimization, the present paper develops a lithography-ready two-qubit module, a compatible nanofabrication process flow, and an experimentally actionable benchmarking program for phonon-mediated entangling operations at 1–4 K.

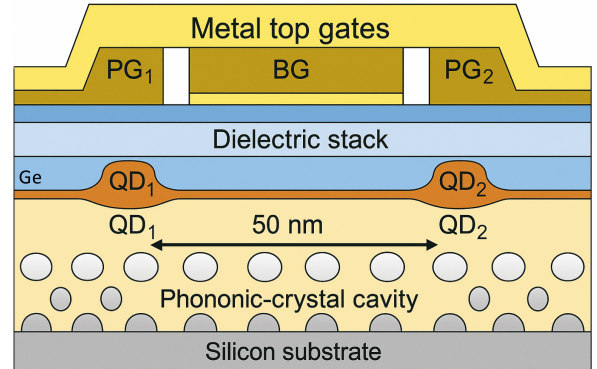


FIG. 1. Conceptual cross-sectional layout of the Ge-based two-qubit module integrated with a PnC cavity. Metal top gates (plunger gates PG<sub>1</sub>, PG<sub>2</sub> and barrier gate BG) are patterned above a dielectric stack and a compressively strained Ge quantum well. Gate-induced depletion in the Ge layer defines two laterally separated hole quantum dots, QD<sub>1</sub> and QD<sub>2</sub>, with center-to-center spacing of  $\sim 50$  nm. The dots reside in a suspended membrane region patterned as a PnC cavity beneath the Ge layer; its engineered acoustic bandgap and localized defect modes spectrally and spatially filter lattice vibrations, enabling controlled phonon-mediated interactions while suppressing leakage into bulk substrate phonons.

## II. DEVICE CONCEPT AND TWO-QUBIT LAYOUT

The two-qubit module consists of a pair of gate-defined hole quantum dots, QD<sub>1</sub> and QD<sub>2</sub>, formed in a compressively strained Ge quantum well grown on a Si substrate and separated from metallic top gates (plunger and barrier gates) by a thin dielectric stack, as shown in Fig. 1. Metallic surface gates locally deplete the high-mobility two-dimensional hole gas (2DHG), defining two lateral quantum dots spaced by approximately 50 nm within the Ge layer. This geometry supports strong tunnel coupling and enables fast, all-electrical spin control via the large spin-orbit interaction intrinsic to Ge.

Crucially, the Ge quantum well is integrated with an underlying PnC cavity patterned into a suspended membrane region. The PnC cavity acts as both a spectral and spatial filter for lattice vibrations: it suppresses coupling to bulk substrate phonons while enhancing interaction with a small number of localized phonon modes that spatially overlap the double-dot region. As a result, phonons confined in the cavity can mediate coherent spin–spin coupling between the two hole-spin qubits and provide additional control parameters—through the phononic bandgap and cavity linewidth—for tailoring dissipation, relaxation, and qubit–environment coupling. Figure 1 summarizes the device concept and introduces the geometric layout analyzed in the following subsections.

The design parameters for the dot size, membrane thickness, and PnC center frequency are not ad hoc but are anchored in the quantitative modeling of spin–phonon

coupling and relaxation presented in Ref. [7]. That work combined a six-band  $k \cdot p$  treatment of strained Ge with Bir–Pikus spin–phonon matrix elements and finite-element (FEM) simulations of PnC defect modes to extract effective  $g$ -factors, spin–phonon coupling strengths  $g_{\text{sp}}$ , and phonon quality factors for realistic gate-defined dots in Ge/SiGe membranes. In the present work, we adopt the same materials parameters and target the optimal operating window identified in Ref. [7], while focusing on a concrete two-qubit layout, a compatible nanofabrication flow, and a measurement-ready experimental program.

### A. Gate-defined hole-spin qubits

The elementary qubit is a single hole confined in a lateral quantum dot formed in a compressively strained Ge quantum well embedded in a  $\text{Si}_{1-x}\text{Ge}_x$  heterostructure. Such Ge/SiGe hole systems combine high-mobility 2DHGs with strong and electrically tunable spin–orbit coupling and have demonstrated stable operation at elevated cryogenic temperatures. [1, 2] Metallic surface gates deposited on a thin dielectric locally deplete the 2DHG, defining quantum dots with in-plane confinement lengths of order 100–150 nm, comparable to those used in recent Ge spin-qubit experiments. [3, 9]

A modest in-plane or out-of-plane magnetic field, typically in the 0.07–0.29 T range, provides the Zeeman splitting for the hole spin. In strained Ge, the effective  $g$ -factor is highly anisotropic and tunable by gate voltage and vertical electric field. [2, 3] The strong spin–orbit interaction enables EDSR, whereby RF voltages applied to selected gates drive coherent spin rotations without requiring local microwave magnetic fields. [3, 12] This all-electrical control paradigm is essential for dense integration and for operation at 1–4 K, where wiring density and cooling power impose practical constraints.

In the two-qubit module, a pair of such quantum dots is defined in close proximity on the shared PnC membrane, as illustrated in Fig. 1. The center-to-center dot spacing of approximately 50 nm is chosen to balance several competing requirements: it is small enough to permit tunable tunnel coupling and capacitive interaction, yet large enough to allow independent gate control and to limit unwanted cross-capacitance. Barrier and plunger gates control the tunnel coupling, dot occupation, and detuning, enabling both single-qubit operation and, if desired, conventional exchange-based two-qubit gates as a complement to phonon-mediated interactions.

### B. PnC cavity and phonon bus

The suspended Ge membrane that hosts the gate-defined quantum dots is patterned into a two-dimensional PnC, thereby realizing a phonon bus for medium-range qubit coupling, as illustrated beneath the Ge layer in

Fig. 1. The PnC consists of a periodic array of holes or pillars that opens a complete acoustic bandgap in the 4–8 GHz range, comparable to structures demonstrated in recent quantum-acoustics and PnC experiments. [4–6] A local perturbation of the lattice—such as a missing or reshaped unit cell—introduces a confined mechanical defect mode whose frequency lies inside the bandgap. This defect mode provides strong spatial confinement and a long phonon lifetime, forming the core element of the phonon-mediated coupling architecture.

Both quantum dots are positioned near a displacement antinode of the defect mode to maximize strain-induced spin–phonon coupling. In Ge hole systems, this coupling arises primarily from strain- and electric-field-induced modulation of the valence-band structure in the presence of strong spin–orbit interaction. [13, 14] When the Zeeman splitting of a qubit is tuned into resonance or near-resonance with the defect-mode frequency, the coupled system is well described by a spin–phonon Jaynes–Cummings Hamiltonian with a coupling rate  $g_{\text{sp}}$  that can reach the MHz scale for realistic mode volumes and strain profiles. [6, 7]

Quantitative estimates of this interaction are obtained from detailed FEM simulations of a 6 GHz defect mode in a triangular Ge PnC combined with the Bir–Pikus spin–phonon Hamiltonian. These simulations yield a normalized strain–qubit overlap of  $\sim 2.6 \times 10^{-2}$  and a single-qubit coupling strength  $g_{\text{sp}} \approx 6$  MHz for realistic dot sizes and vertical electric fields. [7] The same modeling predicts phonon quality factors  $Q \sim 1.8 \times 10^4$  and spin-relaxation times  $T_1 \approx 1$  ms near  $f \approx 6$  GHz, demonstrating that strong, coherent spin–phonon coupling is compatible with long qubit lifetimes.

Guided by the design principles of Ref. [7], we target a phononic bandgap centered in the 2–8 GHz range, corresponding to a lattice constant  $a \simeq v_s/f_{\text{center}} \approx 1.0 \mu\text{m}$  for  $f_{\text{center}} \approx 5$  GHz and a hole radius  $r = (0.2\text{--}0.4)a$ . This choice maximizes both bandgap width and overlap between the phononic strain field and the gate-defined dot wavefunction. Because both qubits couple to the same localized defect mode, phonon exchange—either real or virtual—mediates an effective two-qubit interaction. In the dispersive regime, where the qubits are detuned from the cavity by an amount large compared to  $g_{\text{sp}}$ , this interaction takes the form of a phonon-mediated  $ZZ$  coupling, enabling controlled-phase gates with gate times set by the effective interaction strength and cavity quality factor. [5, 13] In this way, the phonon bus complements short-range exchange interactions, supporting coupling over distances defined by the defect-mode spatial extent (hundreds of nanometers) while preserving the local gate-defined control introduced in Sec. II A.

*a. Effect of sidewall conicity on PnC performance.* In realistic fabrication, dry etching of Ge membranes typically produces sidewalls with a small but finite taper (conicity), leading to hole or trench widths that vary slightly across the membrane thickness. Such sidewall-angle variations modify the local phononic impedance

and can perturb both the phononic bandgap and the confinement of defect modes. In general, conicity reduces the effective bandgap contrast by broadening the distribution of local feature sizes, increasing scattering into continuum modes and lowering the mechanical quality factor  $Q_m$ . Finite-element studies in related PnC platforms indicate, however, that moderate conicity (sidewall angles within a few degrees of vertical) primarily leads to a gradual reduction of  $Q_m$ , rather than a complete loss of the bandgap or defect-mode localization, provided that the nominal bandgap is sufficiently wide.

For the Ge PnC geometries considered here, the targeted bandgap spans several percent in frequency, providing intrinsic tolerance against realistic etch-induced taper. Under these conditions, defect-mode confinement is largely preserved as long as the effective cross-sectional variation remains small compared to the phononic wavelength. In future fabrication iterations, sidewall conicity will be quantitatively characterized using cross-sectional SEM and incorporated into numerical models to refine  $Q_m$  estimates and establish fabrication tolerances for scalable device yield.

### C. Fabrication tolerance and sensitivity analysis

To validate the fabrication-ready nature of the proposed module, we performed FEM sensitivity analyses to quantify the impact of geometric imperfections on PnC performance. The most critical fabrication parameter is the hole radius  $r$ , which determines the fill factor and thus the acoustic bandgap.

Simulations indicate that the design is robust against typical lithographic variations. A radial variation of  $\pm 5\%$  ( $\Delta r \approx \pm 4$  nm) across the lattice results in less than a 10% degradation of the cavity quality factor, while preserving coupling rates sufficient for phonon-mediated interactions. The defect-mode frequency shifts by approximately 150 MHz for a 5% change in radius, well within the tunable bandwidth of the hole-spin Zeeman splitting controlled by the static magnetic field  $B_0$ . These results indicate that standard electron-beam lithography tolerances are sufficient to realize functional devices without requiring post-fabrication trimming.

### D. Operating window at 1–4 K

The combined gate-defined and PnC-based design is optimized for operation in the 1–4 K temperature window, where prior modeling provides clear guidance on achievable performance. Ref. [7] showed that both the effective  $g$ -factor and the spin–phonon coupling can be tuned approximately linearly with vertical electric field,  $g_{\text{eff}}(E_z) = g_0 - \alpha E_z$  and  $g_{\text{sp}}(E_z) = g_{\text{sp},0} + \beta E_z$ , with  $g_0 \approx 2.0$ ,  $\alpha \approx 0.7$  (MV/m) $^{-1}$ ,  $g_{\text{sp},0} \approx 0.5$  MHz, and  $\beta \approx 5.8$  MHz (MV/m) $^{-1}$  for realistic dot geometries. [7] All coupling rates are quoted in MHz as  $g/2\pi$  unless

stated otherwise. This tunability enables Zeeman splittings of several GHz and spin–phonon couplings in the range  $g_{\text{sp}}/2\pi \approx 5$ –10 MHz within experimentally accessible gate-voltage windows.

Using representative values  $g_{\text{sp}}/2\pi \approx 5$ –10 MHz and a detuning  $\Delta/2\pi \sim 100$  MHz, the resulting dispersive two-qubit coupling  $g_{qq} \sim g_{\text{sp}}^2/\Delta$  lies in the range  $g_{qq} \sim 0.25$ –1 MHz, corresponding to controlled-phase gate times well below 1  $\mu$ s and comfortably within the millisecond-scale  $T_1$  values predicted for optimized PnC cavities. [7]

At 1–4 K, the thermal energy  $k_B T$  corresponds to frequencies of approximately 20–80 GHz, so thermal polarization from Zeeman splitting alone is generally weak unless  $\Delta_z/h \gg k_B T/h$ . In practice, initialization at these temperatures is achieved via energy-selective loading/unloading and/or measurement-based protocols, while the Zeeman splitting is chosen primarily to set the qubit frequency and enable spin-selective readout. [15, 16] At these temperatures, high-fidelity single-shot readout enables measurement-based initialization protocols that circumvent the need for strong thermal polarization. For  $g_{\text{eff}} \sim 2$ –4, fields  $B \sim 0.07$ –0.29 T place  $\Delta_z/h$  in the 4–8 GHz band, compatible with PnC defect modes.

Simultaneously, the PnC bandgap must suppress decay into propagating thermal phonons. By placing the qubit transition frequency inside a well-defined acoustic bandgap and coupling it selectively to a high- $Q$  defect mode, decay into the continuum is strongly reduced while retaining a controllable interaction channel. [4, 7] These combined constraints define an operating window in which Zeeman energies, phononic bandgaps, defect-mode frequencies, and the cooling power and wiring constraints of a 1–4 K cryostat are mutually compatible. The two-qubit layout developed here therefore represents a self-consistent, fabrication-ready device concept that can be realized using existing Ge growth and nanofabrication capabilities.

## III. HETEROSTRUCTURE AND MATERIALS STACK

The device concept in Secs. II–IID assumes a high-mobility Ge 2DHG with strong and tunable spin–orbit coupling, integrated with low-noise gate dielectrics and a suspended PnC membrane. In this section, we specify a concrete SiGe/Ge heterostructure and materials stack that can meet these requirements, drawing on recent progress in Ge/SiGe epitaxy and Ge surface passivation for quantum devices and advanced CMOS technology. [2, 17, 18] A schematic of the envisioned stack and its integration with the suspended PnC membrane is shown in Fig. 2.

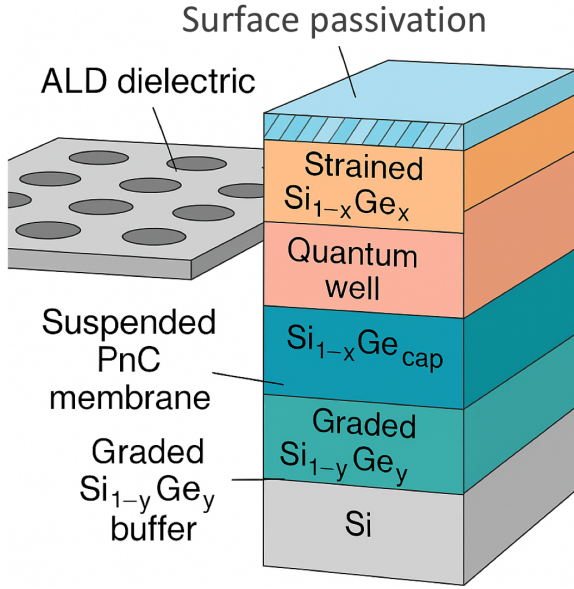


FIG. 2. Illustrative SiGe/Ge heterostructure and materials stack for the PnC-integrated two-qubit device. Right: cross-sectional view of the epitaxial stack, comprising a Si substrate, a graded  $\text{Si}_{1-y}\text{Ge}_y$  buffer that relaxes the lattice, a relaxed  $\text{Si}_{1-x}\text{Ge}_x$  layer that sets the in-plane lattice constant, a compressively strained Ge quantum well hosting the 2DHG, and a SiGe cap, followed by an ALD high- $\kappa$  dielectric and surface passivation layer. Left: a suspended PnC membrane patterned from the same SiGe/Ge stack, hosting the gate-defined quantum dots and the defect cavity.

### A. SiGe/Ge heterostructure

The qubits reside in a compressively strained Ge quantum well grown on a relaxed SiGe virtual substrate, which has emerged as a leading materials platform for planar Ge spin qubits and high-mobility 2DHGs. [2, 19–21] As sketched in Fig. 2, a representative stack consists of (i) a graded  $\text{Si}_{1-y}\text{Ge}_y$  buffer on a Si(001) wafer, in which the Ge fraction is increased gradually to reduce threading-dislocation density; (ii) a relaxed  $\text{Si}_{1-x}\text{Ge}_x$  layer with  $x \simeq 0.7\text{--}0.9$  that sets the in-plane lattice constant; (iii) a 15–20 nm undoped Ge quantum well; and (iv) a SiGe cap that protects the Ge surface during processing and forms part of the suspended PnC membrane. [1, 22–24] Compressive strain in the Ge well modifies the valence-band structure, enhancing the heavy-hole character of the ground state, increasing the out-of-plane effective  $g$ -factor, reducing hyperfine-induced dephasing, and enabling strong, electrically tunable spin-orbit coupling favorable for EDSR-based control. [2, 25]

State-of-the-art Ge/SiGe heterostructures grown by reduced-pressure chemical vapor deposition (RPCVD) or molecular beam epitaxy (MBE) routinely achieve 2DHG mobilities above  $10^5\text{--}10^6 \text{ cm}^2/\text{Vs}$  at millikelvin temperatures and hole densities of order  $10^{11} \text{ cm}^{-2}$ , [17–19, 22] with impurity concentrations in the well and barriers below  $\sim 10^{10} \text{ cm}^{-3}$  as inferred from secondary

ion mass spectrometry and low-temperature Hall measurements. [18, 24] Such low disorder is essential for reproducible quantum-dot formation and for suppressing charge noise in multi-qubit devices.

The structural quality of the virtual substrate and quantum well is typically assessed by high-resolution x-ray diffraction, which confirms the strain state and layer thicknesses, and by cross-sectional transmission electron microscopy, which reveals threading-dislocation densities in the  $10^6\text{--}10^7 \text{ cm}^{-2}$  range and abrupt, well-controlled interfaces. [20, 22] These metrics are consistent with recent demonstrations of gate-defined Ge quantum dots and planar Ge devices coupled to superconducting resonators, [3, 9, 17] supporting the feasibility of the two-qubit, PnC-integrated architecture proposed here.

### B. Surface passivation and gate dielectric

To translate the intrinsic heterostructure quality into low-noise qubits, the exposed Ge (or SiGe) surface must be carefully passivated and covered with a high-quality gate dielectric, as indicated schematically at the top of Fig. 2. Germanium readily forms unstable, defect-rich native oxides; consequently, unpassivated interfaces can exhibit high densities of interface and border traps that drive charge noise and threshold drifts. [2, 26] We therefore adopt an atomic-layer-deposited (ALD) high- $\kappa$  dielectric such as  $\text{Al}_2\text{O}_3$  or  $\text{HfO}_2$ , grown on a chemically cleaned and passivated surface.

For  $\text{Al}_2\text{O}_3$ , effective strategies include wet chemical cleans followed by *in situ* treatments (e.g.,  $\text{H}_2\text{S}$  or  $\text{N}_2/\text{H}_2$  plasmas) that form a thin, controlled  $\text{GeO}_x$  interlayer, followed by ALD  $\text{Al}_2\text{O}_3$ . [27–29] Such stacks can reach interface-state densities  $D_{it}$  in the low  $10^{11} \text{ cm}^{-2}\text{eV}^{-1}$  range and reduced slow-trap densities, as characterized by capacitance–voltage measurements, deep-level transient spectroscopy, and bias-temperature-stress experiments. [30, 31]  $\text{Al}_2\text{O}_3$  further provides a moderate dielectric constant ( $\kappa \sim 9$ ) and wide band gap, enabling strong capacitive coupling to the 2DHG while maintaining low leakage. [32]

$\text{HfO}_2$  is an attractive alternative or complement, offering a higher dielectric constant and broad compatibility with advanced CMOS processing. ALD  $\text{HfO}_2$  grown on suitably prepared Ge surfaces (e.g., with an ultra-thin  $\text{GeO}_2$  or  $\text{Al}_2\text{O}_3$  interlayer) has been shown to form thermally stable interfaces with reduced trap densities and acceptable leakage currents up to typical forming-gas anneal temperatures. [33–35] In both cases, we select dielectric thicknesses in the 5–15 nm range to balance strong gate coupling (supporting fast EDSR and precise dot tuning) against breakdown margins and gate-leakage constraints.

Overall, these surface-passivation and dielectric choices align with those used in recent Ge spin-qubit demonstrations and high-frequency Ge MOS devices, [2, 3, 17] and provide a realistic pathway to achieving the low charge-

noise environment required for phonon-mediated two-qubit operations in the PnC-integrated architecture of Sec. II.

#### IV. NANOFABRICATION PROCESS FLOW

The heterostructure and materials stack described in Sec. III are fully compatible with established planar processing used for Ge spin qubits and high-frequency Ge MOS devices. [3, 9, 17] Here we outline a concrete nanofabrication flow that converts a SiGe/Ge wafer into the two-qubit, PnC-integrated device introduced in Sec. II. The process builds directly on mature gate-defined quantum-dot fabrication in Ge/SiGe, augmented by additional lithography, etching, and release steps required to realize a suspended PnC membrane. [4–6] A schematic overview of the key fabrication steps is shown in Fig. 3.

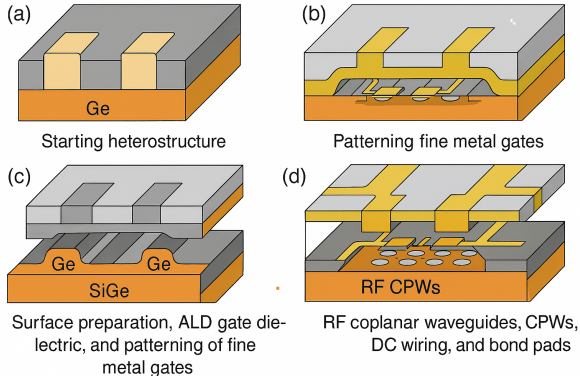


FIG. 3. Illustrative nanofabrication process flow for the Ge-based two-qubit device. (a) Starting SiGe/Ge heterostructure (Sec. III) with definition of mesas and ohmic contacts. (b) Surface preparation, ALD gate dielectric deposition, and patterning of fine metal gates defining the quantum dots and reservoirs. (c) Second aligned lithography and etching steps to form the PnC lattice and defect cavity, followed by selective under-etching to release the suspended membrane. (d) Deposition and patterning of RF coplanar waveguides (CPWs), DC wiring, and bond pads, completing the two-qubit module for packaging and cryogenic measurement.

##### A. Quantum dot and gate patterning

Fabrication begins with definition of active mesas and ohmic contacts on the SiGe/Ge heterostructure wafer. Optical lithography combined with dry or wet etching is used to isolate 50–200  $\mu\text{m}$ -scale mesas that host individual devices. [9, 17] Ohmic contacts to the 2DHG, serving as source, drain, and reservoir regions, are formed by depositing a metal stack such as Pt/Al or Ti/Al, followed by a forming-gas anneal. This step promotes diffusion into

the Ge quantum well and yields low-resistance p-type contacts compatible with cryogenic operation. [17, 18]

After mesa and contact formation, the wafer undergoes a standard RCA-like clean and Ge-specific surface preparation (e.g., HF-last followed by a controlled oxidizing dip), tailored to the gate dielectric selected in Sec. III. A high- $\kappa$  dielectric—typically 5–15 nm of ALD  $\text{Al}_2\text{O}_3$  or  $\text{HfO}_2$ —is then deposited conformally over the wafer. This layer provides both chemical passivation of the Ge surface and the gate insulator for the fine metal gates. [2, 29, 36]

The quantum-dot gates are patterned using high-resolution electron-beam lithography (EBL) with a positive-tone resist (e.g., PMMA or ZEP) or a bilayer stack optimized for liftoff. [3, 9] The gate layout includes plunger gates controlling the electrochemical potential of each dot, barrier gates tuning tunnel couplings to reservoirs and between the two dots, and auxiliary screening or accumulation gates that shape the local electrostatic environment. A typical metal stack is Ti/Pd/Au or Ti/Pt/Au, deposited by electron-beam evaporation to ensure low surface roughness and good step coverage. Ti provides adhesion to the dielectric, Pd or Pt acts as a stable diffusion barrier, and the Au capping layer minimizes series resistance at low temperature. After liftoff, the resulting fine gates have linewidths and spacings in the 20–50 nm range, sufficient to achieve the targeted  $\sim 50$  nm dot separation required for the two-qubit module discussed in Sec. II A. [3]

The gate layout is co-designed to provide largely independent control over dot occupancy, inter-dot detuning, and tunnel coupling while minimizing parasitic capacitance and cross-talk. Three-dimensional electrostatic simulations (e.g., using COMSOL or nextnano) are employed during the design stage to optimize gate widths, overlaps, and spacings, ensuring that small voltage changes on a given gate primarily affect a single control parameter. [2] Such careful electrostatic design is essential for reliable tuning of multi-gate, multi-qubit devices at cryogenic temperatures.

##### B. PnC and membrane patterning

The PnC membrane enabling phonon-mediated coupling is defined in a second, aligned EBL step. The PnC lattice and defect region are patterned in a high-resolution resist layer using alignment marks established during the gate-patterning step, ensuring that the defect-mode antinode coincides with the center of the double-dot structure to within  $\sim 20$  nm. [5]

Following EBL, the PnC pattern—such as a triangular or square lattice of circular holes or an array of pillars—is transferred into the Ge layer by anisotropic reactive-ion etching (RIE). Fluorine- or chlorine-based chemistries are selected to achieve near-vertical sidewalls and minimal surface damage. Comparable pattern-transfer approaches have been used to realize GHz-frequency PnC

cavities in silicon and piezoelectric materials with mechanical quality factors  $Q \gtrsim 10^5$ . [4, 5, 37] For designs requiring a fully suspended membrane, an additional selective undercut step is performed—using, for example,  $\text{XeF}_2$  or TMAH to remove Si, or a wet etch of an underlying sacrificial  $\text{SiO}_2$  layer—while preserving a rigid frame for mechanical support. [6, 38]

Scanning electron microscopy (SEM) is used extensively to verify the realized lattice constant, hole or pillar radius, defect geometry, and alignment relative to the quantum-dot gates. Measured dimensions are incorporated into finite-element-method simulations of the phononic band structure and defect-mode profiles (e.g., using COMSOL or custom FEM codes), enabling iterative refinement of subsequent fabrication runs. [5, 7] This simulation–fabrication feedback loop mirrors best practices in optomechanical and superconducting–acoustic systems and is essential for achieving reproducible bandgaps and strong, well-controlled spin–phonon coupling.

### C. Membrane mechanical stability and risk mitigation

Releasing the suspended Ge/SiGe membrane introduces a critical risk of mechanical instability, most notably buckling or curling, which can directly degrade the phononic performance of the device. Maintaining membrane flatness after removal of the sacrificial layer requires careful control of the strain balance within the heterostructure stack. While the Ge quantum well is intentionally compressively strained to optimize hole-spin properties, the surrounding  $\text{Si}_{1-x}\text{Ge}_x$  layers are engineered with compensating tensile stress so that the net stress in the released membrane is weakly tensile.

Strain balancing is essential because the acoustic properties of the PnC are highly sensitive to geometric deformation. Buckling-induced out-of-plane displacement modifies the effective lattice constant and symmetry of the PnC, shifting the phononic bandgap and defect-mode frequency, potentially by hundreds of MHz. Since the qubit–phonon interaction relies on precise spectral alignment between the defect mode and the qubit Zeeman splitting (typically in the 4–8 GHz range), uncontrolled buckling could render a device inoperable for spin–phonon coupling experiments. To mitigate this risk, we employ stress-compensated growth protocols and verify membrane flatness using optical interferometry or profilometry prior to final device packaging.

### D. RF and DC wiring

A final lithography and metallization step defines the RF and DC wiring required to control and read out the two-qubit module. On-chip coplanar waveguides (CPWs) with a characteristic impedance of  $50 \Omega$  are pat-

terned to route microwave signals to selected gates for electric-dipole spin resonance and to proximal charge sensors or resonators used for qubit readout. [3, 12, 15] The CPWs typically employ a thick Au metallization with a Ti adhesion layer to minimize attenuation and provide robust thermal anchoring at cryogenic temperatures.

DC wiring for gate biases and source–drain contacts is integrated on chip or routed through a custom printed-circuit board (PCB) to which the device is wire-bonded. Large-area Au bond pads around the chip periphery facilitate reliable Al or Au wire bonding to the chip carrier used in a dilution refrigerator or a 1–4 K cryostat. Ground planes and, where required, air bridges are incorporated to suppress slot-line modes and minimize RF cross-talk, following established best practices from spin-qubit and superconducting-qubit architectures. [15, 39] Together, these wiring and packaging steps complete the nanofabrication flow and prepare the device for low-temperature characterization of the phonon-mediated two-qubit interactions introduced in Sec. II B.

## V. READOUT ARCHITECTURE AND SIGNAL CHAIN

The nanofabrication flow in Sec. IV yields a two-qubit module with integrated charge sensor, RF coplanar waveguides, and DC control lines. In this section we describe how these elements are combined into a concrete readout architecture. Our approach follows well-established spin-to-charge conversion protocols developed for GaAs, Si, and Ge spin qubits, [3, 15, 40–42] and leverages RF reflectometry of a proximal sensor dot or quantum point contact (QPC) to enable high-bandwidth, single-shot measurements compatible with operation at 1–4 K. [43–46] An overview of the qubit, sensor, and RF chain is shown schematically in Fig. 4.

### A. Spin-to-charge conversion

The readout sequence converts the spin state of each hole-spin qubit into a charge configuration detectable by the nearby sensor, closely following protocols demonstrated for single-electron and single-hole spins in III–V and group-IV quantum dots. [3, 40–42, 47] Two standard approaches are envisioned:

1. *Energy-selective tunneling (EST):* [40, 47] during readout, a gate pulse rapidly shifts the electrochemical potential of the dot such that only one Zeeman branch (e.g.,  $|\uparrow\rangle$ ) is resonant with a nearby reservoir while the other branch ( $|\downarrow\rangle$ ) remains below the Fermi level. Within a fixed readout window, an  $\uparrow$  spin can tunnel out and be replaced by an opposite-spin hole (or the dot can empty, depending on bias), whereas a  $\downarrow$  spin remains trapped. The final charge state (“occupied” vs “empty” or “reloaded”) is then

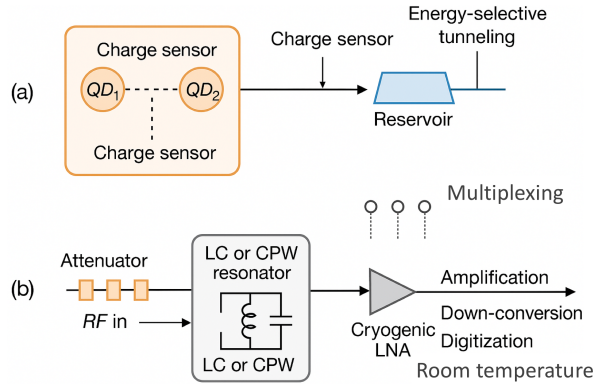


FIG. 4. Illustrative readout architecture and signal chain. (a) Double-dot qubit pair (QD<sub>1</sub>, QD<sub>2</sub>) coupled capacitively to a nearby charge sensor (sensor QD or QPC). Spin-to-charge conversion is performed either by energy-selective tunneling to a reservoir or via Pauli spin blockade between the two dots. (b) The charge sensor is embedded in an RF resonant circuit (LC or CPW resonator) and probed by reflectometry. The input line includes distributed attenuators for thermalization, while the output line passes through a cryogenic low-noise amplifier (LNA) before further amplification, down-conversion, and digitization at room temperature. Multiple resonators can be frequency multiplexed on a single RF line in future multi-qubit devices.

inferred from the charge sensor signal. This method is naturally compatible with the strong tunnel couplings and relatively large Zeeman splittings targeted at 1–4 K.

2. *Pauli spin blockade (PSB)*: [3, 41, 42, 48] here the two-dot system is tuned near a charge transition such as (1, 1)  $\leftrightarrow$  (0, 2), where only singlet states can form the (0, 2) configuration. A gate pulse maps the joint spin state onto either a “blocked” configuration (triplet, remaining in (1, 1)) or an “unblocked” configuration (singlet, transitioning to (0, 2)). The resulting charge configuration is then detected by the sensor as a change in electrostatic potential or current. PSB naturally provides joint (two-qubit) readout and has already been demonstrated in Ge hole double dots. [3, 49]

In both schemes, the spin-relaxation time  $T_1$  in the relevant charge configuration must exceed the measurement integration time to avoid relaxation-induced errors; [40, 47, 50] this requirement informs the design of tunnel couplings, Zeeman energies, and phononic environment described in Secs. II B and II D. The final charge occupancy is then sensed via a proximal charge detector whose conductance is strongly sensitive to the addition or removal of a single hole.

## B. Charge sensor and RF reflectometry

The charge sensor is implemented either as a quantum point contact (QPC) or as an auxiliary quantum dot (sensor dot) located within  $\sim 100$  nm of the qubit pair. QPC-based charge sensing was first demonstrated in GaAs quantum dots, [43] and has since been adapted to Si and Ge platforms, [17, 46] while sensor dots offer enhanced sensitivity and tunability in strongly confined heterostructures. [45, 51]

To reach the high bandwidth and signal-to-noise ratio required for single-shot readout, the sensor is embedded in an RF resonant circuit and probed using RF reflectometry. [44–46] In the simplest implementation, the sensor resistance in series (or parallel) with a lumped inductor forms an *LC* resonator with a resonance frequency  $f_0 = 1/(2\pi\sqrt{LC})$  typically in the 100–500 MHz range. An RF tone near  $f_0$  is injected through a directional coupler on the input line. Changes in the sensor conductance shift the resonant frequency and quality factor, which manifest as changes in the amplitude and phase of the reflected signal  $S_{11}(f)$ .

The reflected tone is amplified and demodulated, and the resulting quadrature signals are integrated over an optimized time window to discriminate the two charge states. This RF-dot or RF-QPC approach routinely achieves sub- $\mu$ s charge-detection times and single-shot spin readout in a variety of platforms. [44–46, 51] In the present architecture, the resonator and sensor are laid out in the same metallization step as the CPWs and bond pads (Sec. IV D), ensuring a compact footprint and low parasitic inductance.

Frequency multiplexing of several resonators on a single RF line is possible by assigning distinct resonance frequencies (separated by a few to tens of MHz) to different sensors and probing them simultaneously with a multi-tone input. [51, 52] This capability will be important for scaling beyond the two-qubit module, but the basic hardware is already compatible with the readout scheme described here.

## C. Link Budget and Readout Fidelity

To validate the feasibility of single-shot readout at elevated temperatures (1–4 K), we perform a link budget calculation estimating the integration time,  $\tau_m$ , required to achieve a readout fidelity of  $\mathcal{F} \geq 95\%$ . Unlike millikelvin operation, the primary noise contribution at 4 K is the system noise temperature, dominated by the thermal noise of the device and the noise equivalent temperature of the cryogenic amplifier chain. We conservatively estimate a total system noise temperature  $T_{\text{sys}} \approx 8$  K (comprising  $\approx 4$  K device noise and  $\approx 4$  K added noise from the LNA and cabling).

For dispersive RF readout, the signal-to-noise ratio (SNR) relates to the reflected signal power difference  $\Delta P_{\text{sig}}$  (the effective signal power contrasting the two

qubit states) and the integration time  $\tau_m$  via:

$$\text{SNR} = \frac{\Delta P_{\text{sig}} \cdot \tau_m}{k_B T_{\text{sys}}} \quad (1)$$

Assuming an input RF power of  $-95$  dBm and a state-dependent reflection coefficient change of  $\Delta\Gamma \approx 0.3$ , we estimate an effective signal power at the amplifier input of  $\Delta P_{\text{sig}} \approx -115$  dBm ( $3.16 \times 10^{-15}$  W).

To distinguish the qubit states with a bit-error rate of  $\epsilon < 5\%$  (corresponding to  $\mathcal{F} > 95\%$ ), we require an SNR threshold of roughly  $\text{SNR} \approx 13$  (assuming Gaussian noise distribution where  $\epsilon = \frac{1}{2}\text{erfc}(\sqrt{\text{SNR}/2})$ ). Solving for the integration time:

$$\tau_m = \frac{\text{SNR} \cdot k_B T_{\text{sys}}}{\Delta P_{\text{sig}}} \approx \frac{13 \cdot (1.38 \times 10^{-23} \text{ J/K} \cdot 8 \text{ K})}{3.16 \times 10^{-15} \text{ W}} \approx 0.45 \times 10^{-15} \text{ s} \quad (2)$$

This yields a required integration time of  $\tau_m \approx 450$  ns. Even with a more conservative assumption of  $\Delta P_{\text{sig}} \approx -125$  dBm, the integration time increases to  $\approx 4.5 \mu\text{s}$ . Importantly, this timescale is well within the expected spin relaxation time  $T_1$  for Ge hole spins, which typically exceeds  $10\text{--}100 \mu\text{s}$  at these temperatures when protected by the phononic bandgap, ensuring that the qubit state is preserved during the measurement window.

#### D. Cryogenic RF chain

The RF reflectometry signal chain follows best practices developed for semiconductor spin qubits and superconducting qubits. [15, 39, 44] On the input side, the RF drive is heavily attenuated and filtered at multiple temperature stages (e.g., 300 K, 40 K, 4 K, and base temperature) to both set the desired power at the device and thermalize noise from room-temperature electronics. Typical configurations use 40–60 dB of total attenuation, split across stages to avoid excessive local heating.

On the output side, the reflected RF signal passes through an isolator or circulator to protect the device from back-propagating amplifier noise, then is amplified by a cryogenic low-noise amplifier (LNA) mounted at the 4 K stage or, in higher-performance setups, at the base plate. Commercial LNAs operating in the 50–500 MHz range achieve noise temperatures of a few kelvin with gains of 30–40 dB, [39, 53] which is compatible with our 1–4 K operating window and modest drive powers.

After further amplification and filtering at room temperature, the signal is down-converted in an IQ mixer referenced to the same local oscillator used to generate the probe tone. The resulting in-phase ( $I$ ) and quadrature ( $Q$ ) components are digitized by a fast ADC and processed in real time (e.g., in an FPGA) or off-line on a computer to extract the spin state via thresholding or maximum-likelihood classification. [45, 51] The same RF chain can be straightforwardly extended to multiple sensors through frequency multiplexing, as mentioned above.

#### E. Expected readout performance

For realistic sensor operating points (transconductance of order  $10^{-3}\text{--}10^{-2}$  S), resonator quality factors  $Q \sim 50\text{--}200$ , and cryogenic LNA noise temperatures of a few kelvin, we expect single-shot spin readout fidelities exceeding 95% with integration times of a few microseconds. [40, 46, 50, 54] These estimates are consistent with experimental demonstrations of RF-based spin readout in GaAs, Si, and Ge systems, which achieve  $\mathcal{F} \gtrsim 97\%$  for integration times between 1 and 10  $\mu\text{s}$  depending on device parameters and temperature. [3, 15, 46]

A simple signal-to-noise analysis shows that the minimum integration time  $t_{\text{int}}$  scales approximately as  $t_{\text{int}} \propto (T_n/6P_{\text{sig}})(1/\Delta G^2)$ , where  $T_n$  is the amplifier noise temperature,  $P_{\text{sig}}$  is the RF power at the resonator, and  $\Delta G$  is the conductance change of the sensor between the two charge states. [45, 54] Thus, improvements in sensor design (larger  $\Delta G$ ), resonator engineering (higher  $Q$  and coupling efficiency), and cryogenic amplification (lower  $T_n$ ) directly translate into shorter readout times and higher fidelities.

Importantly, the required RF drive powers remain modest (typically below  $\sim -90$  dBm at the device), so that readout heating is compatible with the thermal budget of a 1–4 K platform and does not significantly perturb the phononic environment engineered in Sec. II B. Once actual devices are fabricated, these performance estimates can be refined by measuring the noise spectra, resonator response, and spin-relaxation times under operating conditions, but existing experiments suggest that high-fidelity, single-shot readout is well within reach for the proposed architecture.

## VI. CRYOGENIC MEASUREMENT SETUP

The readout architecture described in Sec. V is implemented in a cryogenic measurement environment that provides low-noise electrical access, a well-controlled magnetic field, and stable operation in the 1–4 K temperature window targeted for this Ge hole-spin platform. The setup follows best practices established for semiconductor spin qubits and superconducting circuits, [39, 44, 52] with wiring, filtering, and thermal anchoring tailored to RF reflectometry and phonon-mediated control. A schematic overview is shown in Fig. 5.

The fabricated chip (Sec. IV) is mounted on a gold-plated copper PCB or a low-loss ceramic carrier and wire-bonded to the DC and RF bond pads. The carrier is then thermally anchored to the cold stage of a cryostat capable of reaching 1–4 K, such as a pumped  $^4\text{He}$  system or a closed-cycle  $^4\text{He}$  cryostat with a low-vibration sample plate. [15, 16, 39] To minimize microphonic pickup and ensure robust thermalization, the carrier is clamped or bolted with high-conductivity interfaces (e.g., indium gaskets or thermally conductive foils), and bond-wire lengths are kept as short as practical.

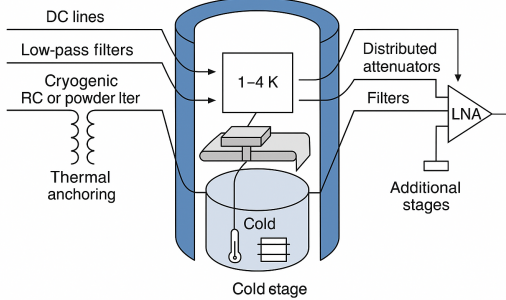


FIG. 5. Illustrative cryogenic measurement setup for the Ge-based two-qubit device. The chip is wire-bonded to a PCB or ceramic carrier mounted on the cold stage of a 1–4 K cryostat inside a superconducting magnet. DC gate and bias lines (left) pass through room-temperature low-pass filters, cryogenic RC or powder filters, and thermal anchoring stages before reaching the chip. RF lines for EDSR and reflectometry (right) are routed through distributed attenuators and filters on the input side and through a cryogenic low-noise amplifier (LNA) and additional stages on the output side. Thermometers and heaters on the sample stage provide temperature control and stabilization over the 1–4 K range.

DC gate voltages and source/drain biases are supplied by low-noise voltage sources at room temperature. Their outputs pass through feedthrough  $\pi$ -filters or RC low-pass filters at the cryostat entry, followed by additional cryogenic filtering (e.g., lumped-element RC filters, copper-powder filters, or lossy coaxial lines) anchored at intermediate stages (40 K and 4 K) before reaching the sample. [44, 55, 56] This staged filtering suppresses broadband electromagnetic interference and reduces low-frequency charge noise that would otherwise broaden the qubit resonance and limit  $T_2^*$  and readout fidelity.

RF signals for EDSR and reflectometry readout (Sec. V) are routed using semi-rigid coaxial cables with well-characterized attenuation and thermal conductivity. [39, 44] On the input side, cascaded attenuators (typically totaling 40–60 dB) are distributed across temperature stages (300 K, 40 K, 4 K, and the cold stage) to thermalize room-temperature noise and set the desired RF power at the device while limiting dissipation on the cold plate. To suppress out-of-band noise and spurious mixer products, absorptive (e.g., Eccosorb) or commercial band-pass filters can be placed close to the sample. [39]

On the output side, the reflected RF signal from the sensor resonator (Sec. V B) passes through an isolator or circulator anchored at 4 K to reduce back-propagating amplifier noise, and is then amplified by a cryogenic LNA with a noise temperature of a few kelvin. [57, 58] Subsequent amplification, filtering, and IQ down-conversion are performed at room temperature as described in Sec. V D, after which the signal is digitized and processed

to infer the charge (and hence spin) state.

A static magnetic field is provided by a superconducting solenoid or vector magnet surrounding the sample space. The field magnitude and orientation are selected to exploit the anisotropic and gate-tunable  $g$ -factor in Ge hole-spin qubits while limiting unwanted orbital effects that can degrade confinement and stability. [2, 3, 25] In practice, in-plane fields of 0.07–0.29 T are sufficient to reach Zeeman splittings in the several-GHz range needed for operation at 1–4 K (Sec. IID). [15, 16]

Finally, calibrated thermometry (e.g., Cernox or RuO<sub>2</sub> sensors) and resistive heaters mounted near the sample enable closed-loop temperature stabilization and controlled sweeps across the 1–4 K range. [39] These capabilities are essential for mapping temperature-dependent coherence and readout performance and for validating that the engineered phononic environment remains stable under realistic drive and operating conditions. Together, the cryogenic infrastructure, wiring, and magnetic-field control provide a complete experimental platform for characterizing the phonon-mediated two-qubit operations proposed in this work.

## VII. EXPERIMENTAL PROGRAM AND TARGET METRICS

We take the optimized operating window and spin-phonon parameters identified in Ref. [7] as inputs and translate them here into concrete design rules and experimentally testable benchmarks for a two-qubit module. The cryogenic infrastructure in Sec. VI and the readout architecture in Sec. V provide the key ingredients needed to execute this program. Our measurement sequence proceeds from charge tuning and noise baselining, through single-qubit control and PnC validation, and culminates in spectroscopic and time-domain signatures of two-qubit coupling. The workflow follows established protocols developed in GaAs, Si, and Ge spin-qubit experiments, [3, 15, 40, 47, 48] but is structured to isolate and quantify the role of the engineered phononic environment. Figure 6 sketches representative data products, while the corresponding quantitative targets—guided by Ref. [7]—are summarized in Table I.

### A. Charge stability and tuning

The first stage is to establish robust electrostatic control of the double dot in the few-hole regime and to verify reliable RF readout via the proximal charge sensor. We will adapt standard charge-sensing methods developed for GaAs and Si double dots [40, 43, 45] to the Ge/SiGe platform by sweeping pairs of gate voltages while monitoring the demodulated RF reflectometry signal (Sec. V B). The resulting charge stability diagrams should exhibit the characteristic honeycomb pattern of a double dot, with well-resolved addition lines correspond-

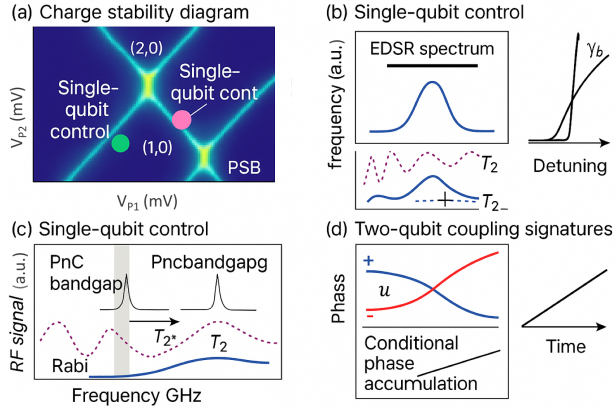


FIG. 6. Illustrative data and target metrics for the experimental program. (a) Charge stability diagram measured via RF sensing, showing few-hole charge transitions and a double-dot honeycomb pattern; operating points for single-qubit control and Pauli spin blockade (PSB) are indicated. (b) Single-qubit control: EDSR spectra and time-domain traces (Rabi, Ramsey, echo) used to extract  $g$ -factors and coherence times  $T_2^*$  and  $T_2$  in the 1–4 K window. (c) Phononic-cavity spectroscopy: spin-relaxation time  $T_1$  versus Zeeman energy, revealing suppression inside the PnC bandgap and peaks near the defect-mode frequency that yield the effective spin–phonon coupling strength  $g_{sp}$ . (d) Two-qubit coupling signatures: avoided crossings in the joint spectrum and conditional phase accumulation in time-domain experiments, from which an effective two-qubit coupling rate and entangling-gate fidelity can be inferred.

ing to changes in the occupations of QD<sub>1</sub> and QD<sub>2</sub>, as illustrated in Fig. 6(a).

An early milestone is to reach the (0,0) charge state and then step into the (1,0), (0,1), and (1,1) configurations, confirming single-hole control in each dot, as demonstrated in prior Si and Ge spin-qubit experiments. [3, 9, 47] From these data we will extract gate lever arms, charging energies, and inter-dot capacitive coupling, which in turn define operating points for single-qubit control and for PSB readout (Sec. V A). Charge-noise levels can be quantified by tracking temporal fluctuations of selected charge transitions, yielding an effective charge-offset noise amplitude and spectral density that can be compared across devices and materials systems. [56, 59] These electrostatic and noise metrics provide the baseline against which the coherence and phonon-engineering benchmarks in Table I will be evaluated.

## B. Impact of Suspension on Dephasing and Surface Passivation

Suspending the Ge/SiGe membrane is essential for phonon confinement and the formation of well-defined phononic bandgaps, but it also introduces new coherence challenges. Compared to bulk or substrate-supported

heterostructures, suspension increases the surface-to-volume ratio and exposes additional interfaces that can host fluctuating charge traps. In bulk devices, the active quantum well is separated from the substrate interface by several micrometers, whereas in the suspended geometry the underside of the membrane is exposed and lies only  $\sim$ 100–200 nm from the hole wavefunction. Surface states and dangling bonds at this semiconductor–vacuum interface can generate low-frequency ( $1/f$ ) electric-field noise that couples efficiently to hole spins via strong spin–orbit interactions.

If left untreated, this additional noise channel could reduce  $T_2^*$  by a factor of 2–5 relative to bulk reference devices, depending on the areal trap density and fluctuation spectrum. Similar surface-induced dephasing has been reported in other suspended semiconductor nanostructures and is expected to be particularly relevant for hole-based qubits, which are intrinsically more sensitive to electric-field noise.

To mitigate these effects, we implement a dedicated bottom-surface passivation strategy based on atomic layer deposition (ALD) of a thin, conformal dielectric on the underside of the membrane. ALD-grown Al<sub>2</sub>O<sub>3</sub> and HfO<sub>2</sub> are established passivation layers for Ge-based devices, providing chemical passivation of dangling bonds and electrostatic screening of charge fluctuations. In particular, Al<sub>2</sub>O<sub>3</sub> deposited using trimethylaluminum (TMA) and water precursors can form stable Ge–O bonds at the interface, while HfO<sub>2</sub> offers a higher dielectric constant that can further reduce the impact of remote charge traps.

We are evaluating two complementary ALD process flows. In the first, a thin bottom dielectric ( $\sim$ 5–10 nm) is deposited *prior* to membrane release, provided the sacrificial layer chemistry and release selectivity allow. This “pre-passivation” route deposits the dielectric while the stack remains mechanically supported, improving film uniformity and avoiding stiction during release. The sacrificial layer is then selectively removed, leaving a suspended membrane with a pre-passivated bottom surface. When compatible with the release process, this approach minimizes mechanical stress and is the preferred option.

In the second flow, ALD passivation is performed *after* membrane release to directly treat the exposed underside. Because ALD is intrinsically conformal and can be performed at moderate temperatures ( $\lesssim$  200 °C), it is well suited for coating high-aspect-ratio phononic-crystal features. To prevent collapse during wet processing, the post-release sequence incorporates anti-stiction drying techniques such as critical point drying or vapor-phase drying, which are widely used in MEMS/NEMS fabrication and are compatible with the membrane dimensions considered here.

The impact of passivation on coherence will be quantified through systematic  $T_2^*$  measurements on suspended devices with and without bottom-surface ALD, benchmarked against control qubits fabricated on unreleased (bulk-supported) regions of the same wafer. This con-

trolled comparison isolates the dephasing contribution associated with suspension and directly assesses passivation efficacy, informing the dielectric choice and process sequence for future multi-qubit phononic architectures.

*a. Thermalization of the suspended membrane.* Suspension also alters the thermal environment and must be engineered to ensure stable operation at 1–4 K. In steady state, the local temperature rise near the dots can be estimated as  $\Delta T \approx P_{\text{diss}}/G_{\text{th}}$ , where  $P_{\text{diss}}$  is the RF and DC power dissipated in the gates and quantum well, and  $G_{\text{th}}$  is the effective thermal conductance to the anchored frame through the suspension tethers and metallization. For micron-scale Ge membranes with multiple tethers at cryogenic temperatures,  $G_{\text{th}}$  can be engineered in the range  $10^{-8}$ – $10^{-6}$  W/K, depending on tether geometry, thickness, and surface scattering. In this regime, pW-level dissipation produces sub-mK to sub-0.1 K temperature increases, while nW-level dissipation remains compatible with operation in the 1–4 K window provided adequate thermalization pathways are incorporated.

Although the PnC bandgap suppresses phonon propagation near the localized defect-mode frequency used for coherent coupling, thermal transport at cryogenic temperatures is broadband. Heat can therefore still flow through phonon modes outside the bandgap unless the structure is deliberately over-isolated. To avoid creating a thermal bottleneck, the design includes thermal bypass pathways, such as unpatterned sections of the suspension tethers and continuous metal ground planes or straps, which provide additional phononic and electronic heat flow to the bulk frame. These features help ensure that the phononic structure functions as a coherent coupling element rather than a heat trap.

Local heating will be assessed experimentally by monitoring drive-dependent shifts and linewidth broadening of qubit resonances and phononic features, and by comparing pulsed and continuous-drive protocols. Together, these measurements will establish an operating envelope in which the effective phonon temperature seen by the qubits remains close to the stage temperature and consistent with the system noise temperature assumed in the RF link budget.

### C. Single-qubit control and coherence

With stable single-hole occupancy established, we characterize single-qubit control using EDSR, as outlined in Sec. V A. At fixed magnetic field, microwave-frequency gate drives are applied to a selected plunger or barrier gate, and the spin state is read out via energy-selective tunneling or PSB. [3, 40, 41] Frequency sweeps yield resonance peaks from which we extract effective  $g$ -factors for QD<sub>1</sub> and QD<sub>2</sub>. Repeating these measurements as a function of gate bias and electric-field configuration maps the anisotropy and tunability of the hole  $g$ -tensor in the realized device geometry. [2, 25]

Time-domain control experiments—Rabi oscillations,

Ramsey fringes, Hahn echo, and, where useful, Carr–Purcell–Meiboom–Gill (CPMG) sequences—quantify coherence in the 1–4 K window. [3, 15, 48, 50] From these data we extract the inhomogeneous dephasing time  $T_2^*$ , the echo coherence time  $T_2$ , and the EDSR Rabi frequency for realistic drive amplitudes, as illustrated in Fig. 6(b). Systematic sweeps versus temperature and field orientation will help identify dominant decoherence mechanisms (e.g., charge noise, phonon-induced dephasing, or residual hyperfine coupling) and quantify the benefit of the phonon-engineered environment. [13, 60, 61]

A practical near-term target is  $T_2^* \gtrsim 1 \mu\text{s}$  and  $T_2 \gtrsim 10$ – $50 \mu\text{s}$  at operating points where single-qubit gate times (set by the Rabi frequency) lie in the 10–100 ns range. Achieving these figures of merit, together with the spin–phonon parameters in Table I, would place the device in a regime compatible with phonon-mediated coupling studies and broadly competitive with Si and Ge spin-qubit implementations at comparable temperatures. [3, 15, 16]

### D. PnC characterization

Direct spectroscopy of GHz phononic modes is non-trivial in the present architecture, so we characterize the PnC cavity primarily through its imprint on spin relaxation and dephasing. The central measurement is the spin-relaxation time  $T_1$  as a function of Zeeman energy, obtained by sweeping the magnetic field while tuning the qubit transition frequency within, across, and outside the designed PnC bandgap. [4–7] Representative signatures are sketched in Fig. 6(c).

In the absence of a phononic bandgap,  $T_1(B)$  is expected to follow a power law determined by bulk phonon emission mediated by spin–orbit coupling. [61, 62] When the qubit frequency lies inside the PnC bandgap, decay into propagating phonons should be suppressed, yielding an enhanced  $T_1$  plateau. As the Zeeman energy is tuned into resonance with the localized defect mode,  $T_1$  should decrease sharply due to resonant coupling; the amplitude and linewidth of this feature provide experimental access to the spin–phonon coupling rate  $g_{\text{sp}}$  and the mechanical quality factor  $Q_{\text{m}}$ . [5, 6, 13]

These measurements will be compared against finite-element simulations of the PnC band structure and defect-mode strain profiles, together with analytical models of spin–phonon coupling in strained Ge quantum wells. [7, 13, 25] A key benchmark (Table I) is to demonstrate at least an order-of-magnitude enhancement of  $T_1$  within the bandgap relative to frequencies just outside it, while maintaining  $g_{\text{sp}}/2\pi$  in the  $\sim 0.5$ – $5$  MHz range required for practical phonon-mediated gates.

### E. Two-qubit coupling signatures

The final phase of the program is to identify and quantify phonon-mediated coupling between the two hole-spin qubits. With both dots tuned to single-hole occupancy and coupled to the same defect mode (Sec. II B), we pursue two complementary approaches corresponding to Fig. 6(d) and the coupling targets in Table I.

First, two-qubit spectroscopy probes static interaction signatures. By sweeping drive frequency and magnetic field (or by independently tuning the two qubits via gate-induced  $g$ -factor shifts), we map the joint spectrum and search for avoided crossings or conditional frequency shifts that depend on the partner-qubit state. [48, 63, 64] The size of these features yields an effective coupling strength  $J_{\text{eff}}$ , which can be benchmarked against dispersive-coupling expectations based on the measured  $g_{\text{sp}}$  and the detuning from the defect mode. [7, 13]

Second, time-domain experiments quantify dynamical entangling interactions. Candidate protocols include (i) conditional phase accumulation, in which one qubit is prepared in  $|\uparrow\rangle$  or  $|\downarrow\rangle$  and the phase evolution of the partner qubit is monitored, [63, 64] and (ii) echo-based sequences that refocus single-qubit dephasing while retaining two-qubit  $ZZ$  interactions. From these measurements we extract an effective entangling-gate rate (e.g., the time to accumulate a controlled- $Z$  phase of  $\pi$ ) and compare it to measured  $T_2$  and  $T_1$  values to build an initial gate-error budget.

A key benchmark, consistent with the dispersive estimates in Sec. II D and Table I, is to achieve  $J_{\text{eff}}/2\pi$  in the few-hundred-kHz to MHz range while maintaining coherence sufficient to support entangling-gate fidelities above 90–95% in early devices, with a clear path to improvement through cavity optimization, materials refinement, and advanced control. Comparing phonon-mediated coupling to alternative mechanisms such as direct exchange, capacitive coupling, or superconducting resonators [48, 65, 66] will inform the design of larger-scale Ge-based quantum processors and phonon-enabled sensor architectures.

## VIII. DISCUSSION AND OUTLOOK

While the design targets outlined here are compatible with current Ge/SiGe growth and PnC fabrication capabilities, realizing the required phonon  $Q$ -factors and reproducible defect-mode frequencies will still demand careful process control. In particular, membrane thickness, feature dimensions (hole radii and lattice constant), and etch-induced surface roughness all directly impact the bandgap, scattering losses, and mode localization. Likewise, operation at 1–4 K places practical constraints on continuous RF drive: EDSR and reflectometry powers must be chosen to achieve adequate signal-to-noise ratio without introducing excessive local heating or destabilizing charge configurations. These considerations are not

unique to Ge, but they will set the operating envelope for first-generation demonstrations based on the present module.

The experimental program in Sec. VII provides a step-wise path from basic charge characterization to signatures of phonon-mediated two-qubit coupling. Together with the cryogenic infrastructure and readout chain described in Secs. V and VI, the result is a self-consistent, experimentally realizable architecture that tightly links materials engineering, phonon design, nanofabrication, and RF control. Rather than proposing an abstract family of devices, we converge on a specific geometry, operating window, and readout scheme that can be pursued with existing Ge/SiGe growth and nanofabrication capabilities at multiple laboratories worldwide. [2, 3, 17]

From a materials and device perspective, the two-qubit module leverages the key advantages of strained Ge hole systems—large and electrically tunable spin-orbit coupling, compatibility with 1–4 K operation, and Si-compatible processing—while explicitly addressing historically challenging issues such as charge noise and phonon-induced relaxation through optimized dielectrics and PnC engineering. [2, 5, 7, 26] A successful demonstration of enhanced  $T_1$  and robust  $T_2$  within the PnC bandgap would not only validate the design choices in Secs. II B and VII D, but would also establish a transferable strategy for phonon engineering in other spin-qubit platforms.

Several natural extensions follow from the present design. On the device side, integrating superconducting microwave resonators or high-impedance transmission lines with the PnC membrane would enable hybrid spin-phonon-photon architectures, in which localized mechanical modes couple both to spins and to microwave photons for long-range interconnects and multiplexed readout. [4, 6, 65, 66] Such hybrid devices could exploit the strong spin-phonon interaction of hole spins together with electromechanical coupling in nanostructured Ge to access high-cooperativity tripartite interactions, opening routes to phononic transduction and mechanically protected quantum memories.

On the phonon-design side, alternative PnC motifs and defect geometries—including snowflake lattices, bound states in the continuum, and topological edge modes—may offer higher intrinsic  $Q_m$ , larger bandgaps, or reduced sensitivity to fabrication disorder compared with the baseline cavity of Sec. II B. [5, 37, 38] Systematic comparison of measured  $T_1(B)$  spectra with refined finite-element models will guide these iterations, with the goal of simultaneously maximizing  $T_1$  deep in the bandgap while preserving MHz-scale spin-phonon coupling needed for fast entangling operations.

At the system level, scaling beyond a single two-qubit module will require coordinated progress in wiring, calibration, and architectural design. Linear chains or two-dimensional arrays of phonon-coupled Ge qubits could be constructed by repeating the module and coupling multiple cavities or defect modes on a shared membrane,

TABLE I. Key target parameters for the two-qubit module, informed by the modeling of Ref. [7] and used to guide the experimental program outlined in Sec. VII.

Quantity	Target value	Rationale
Phonon frequency $f_{\text{mode}}$	5–6 GHz	Balance strong coupling and long lifetime
Phonon $Q$ -factor $Q_m$	$\gtrsim 1.5 \times 10^4$	Finite-element modeling of the PnC cavity
Spin–phonon coupling $g_{\text{sp}}/2\pi$	5–10 MHz	Bir–Pikus coupling with realistic mode volume
Relaxation time $T_1$	$\sim 1$ ms at 6 GHz	Bandgap protection with engineered defect mode
Two-qubit coupling $g_{\text{qq}}/2\pi$	0.25–1 MHz	Dispersive scaling $g_{\text{sp}}^2/\Delta$

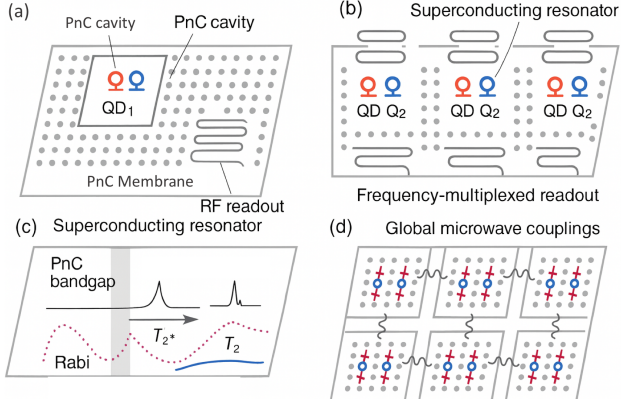


FIG. 7. Conceptual outlook for the Ge phonon-coupled architecture. (a) The two-qubit module developed in this work, combining a PnC cavity, double-dot qubits, and RF readout. (b) Extension to a linear chain of modules on a shared PnC membrane, with frequency-multiplexed readout resonators. (c) Integration of superconducting resonators for hybrid spin–phonon–photon coupling and long-range entanglement. (d) Vision of a two-dimensional array of modules with local phononic couplings and global microwave interconnects, suitable for quantum computing and quantum-sensing applications.

while frequency-division multiplexing of RF sensors and integration of cryogenic control electronics can mitigate wiring overhead. [39, 52, 67] Achieving stable operation in larger arrays will also require cross-talk mitigation, robust calibration workflows, and pulse sequences tailored to the decoherence budgets identified in Secs. VII C and VII E. Figure 7 sketches representative directions along these lines.

Overall, the two-qubit module proposed here represents a natural and experimentally accessible next step toward phonon-coupled Ge hole-spin qubits as a practical platform for quantum computation and quantum sensing at moderate cryogenic temperatures. By anchoring the discussion in a concrete device geometry, measurement workflow, and quantitative performance targets, this work provides a clear near-term roadmap while leaving ample room for innovation in materials, phonon engineering, and scalable system architectures.

## IX. CONCLUSION

We have presented a concrete device architecture for phonon-coupled Ge hole-spin qubits that integrates a high-mobility strained Ge/SiGe heterostructure, a suspended PnC cavity, gate-defined double quantum dots, and RF-reflectometry-based readout. Building on recent advances in Ge materials and spin-qubit platforms that demonstrate fast, high-fidelity control in planar Ge/SiGe heterostructures, [2, 3, 17] our design specifies a realistic materials stack, nanofabrication process, and cryogenic measurement environment targeted at operation in the 1–4 K regime. The resulting two-qubit module is therefore not an abstract proposal, but a well-defined experimental system that can be fabricated and benchmarked using currently available infrastructure.

A central element of the architecture is the integration of the qubits into a defect cavity of a two-dimensional PnC patterned directly into the Ge membrane. Inspired by advances in optomechanical and quantum-acoustic systems, [4–6, 37] the PnC bandgap and defect mode are engineered to suppress decay into bulk phonons while enabling strong, spectrally selective spin–phonon coupling. We have outlined a comprehensive experimental program that employs established spin-to-charge conversion and RF sensing techniques [15, 40, 45] to characterize charge stability, single-qubit coherence, phonon-modified relaxation, and ultimately phonon-mediated two-qubit interactions within this engineered phononic environment.

On the benchmarking side, we identified concrete and experimentally accessible target metrics—including single-hole control in each dot,  $T_2^*$  and  $T_2$  in the microsecond to tens-of-microseconds range, enhanced  $T_1$  within the PnC bandgap, and two-qubit coupling rates in the few-hundred-kHz to MHz regime—that would place this platform on competitive footing with existing Si and Ge spin-qubit implementations operating at comparable temperatures. [3, 15, 16, 48] Because the architecture is compatible with frequency-multiplexed RF readout and with the integration of on-chip superconducting resonators, [52, 65, 66] it naturally supports extensions toward hybrid spin–phonon–photon systems and scaled arrays of Ge qubits.

Looking ahead, the two-qubit module developed here can serve as a foundational building block for larger-scale quantum processors and quantum sensors based on

Ge. Systematic exploration of alternative PnC geometries, cavity designs, and coupling schemes—guided by the experimental benchmarks proposed in Sec. VII—will clarify the advantages and trade-offs of phonon-mediated interactions relative to more conventional exchange or capacitive coupling mechanisms. [13, 65, 66] More broadly, the design philosophy articulated in this work—explicit co-design of materials, phonons, and qubits; careful attention to fabrication and measurement constraints; and the use of quantitative, testable performance targets—extends beyond Ge and may help guide the development of other solid-state platforms in which phonons are engineered as a resource rather than treated solely as a source of decoherence.

In summary, the proposed Ge phonon-coupled two-qubit architecture provides a clear, experimentally

grounded route toward exploiting engineered mechanical modes for coherent control and entanglement of spin qubits at accessible cryogenic temperatures. Its successful realization would represent an important step toward unifying quantum information processing with quantum acoustics and toward deploying Ge-based quantum devices for both computing and sensing applications.

## ACKNOWLEDGMENTS

This work was supported in part by NSF OISE 1743790, NSF PHYS 2117774, NSF OIA 2427805, NSF PHYS 2310027, NSF OIA 2437416, DOE DE-SC0024519, DE-SC0004768, and a research center supported by the State of South Dakota.

---

[1] H. Watzinger, J. Kukucka, L. Vukušić, C. Kloeffel, M. Veldhorst, D. Loss, and G. Katsaros, *Nature Communications* **9**, 3902 (2018).

[2] G. Scappucci, C. Kloeffel, F. A. Zwanenburg, D. Loss, M. Myronov, J.-J. Zhang, S. De Franceschi, G. Katsaros, and M. Veldhorst, *Nature Reviews Materials* **6**, 926 (2021).

[3] N. W. Hendrickx, W. I. L. Lawrie, M. Russ, F. van Rijgelen, S. L. de Snoo, R. N. Schouten, A. Sammak, G. Scappucci, and M. Veldhorst, *Nature* **577**, 487 (2020).

[4] Y. Chu, P. Kharel, W. H. Renninger, L. D. Burkhardt, L. Frunzio, P. T. Rakich, and R. J. Schoelkopf, *Science* **358**, 199 (2017).

[5] P. Arrangoiz-Arriola, E. A. Wollack, Z. Wang, M. Pechal, W. Jiang, M. Reagor, J. Aumentado, J. Vuckovic, and A. H. Safavi-Naeini, *Nature* **571**, 537 (2019).

[6] A. Bienfait, K. J. Satzinger, Y. P. Zhong, H.-S. Chang, M.-H. Chou, A. N. Cleland, *et al.*, *Science* **364**, 368 (2019).

[7] D.-M. Mei, S. A. Panamaldeniya, K.-M. Dong, S. Bhattarai, N. Budhathoki, and A. Warren, *Quantum Science and Technology* **10**, 045067 (2025).

[8] D.-M. Mei, N. Budhathoki, S. A. Panamaldeniya, K.-M. Dong, S. Bhattarai, A. Warren, A. Prem, and S. Chhetri, *Physics of the Dark Universe* **50**, 102165 (2025).

[9] W. I. L. Lawrie, T. McJunkin, N. W. Hendrickx, A. Sammak, G. Scappucci, and L. M. K. Vandersypen, *Applied Physics Reviews* **7**, 041304 (2020).

[10] H. J. Kimble, *Nature* **453**, 1023 (2008).

[11] S. Wehner, D. Elkouss, and R. Hanson, *Science* **362**, eaam9288 (2018).

[12] L. C. Camenzind *et al.*, *Nature Electronics* **5**, 178 (2022).

[13] M. Benito, M. Niklas, and G. Burkard, *Physical Review B* **100**, 125430 (2019).

[14] G. D. Mahan, *Many-Particle Physics*, 2nd ed. (Springer, 1990).

[15] L. Petit *et al.*, *Nature* **580**, 355 (2020).

[16] C. H. Yang *et al.*, *Nature* **580**, 350 (2020).

[17] Y.-X. Li, Z. Kong, S. Hou, G. Wang, and S. Huang, *Physical Review B* **108**, 045303 (2023).

[18] Z. Kong, Z. Li, G. Cao, *et al.*, *ACS Applied Materials & Interfaces* **15**, 28799 (2023).

[19] T. Tanaka, O. Nakatsuka, N. Taoka, *et al.*, *Applied Physics Letters* **100**, 222102 (2012).

[20] M. Myronov, K. Sawano, Y. Shiraki, T. Mouri, and K. M. Itoh, *Applied Physics Letters* **91**, 082108 (2007).

[21] M. A. Zudov, O. A. Mironov, Q. A. Ebner, P. D. Martin, Q. Shi, and D. R. Leadley, *Physical Review B* **89**, 125401 (2014).

[22] A. Sammak, D. Sabbagh, N. W. Hendrickx, *et al.*, *Advanced Functional Materials* **29**, 1807613 (2019).

[23] L. Ruggiero, A. Nigro, I. Zardo, and A. Hofmann, *Nano Letters* **24**, 13263 (2024), arXiv:2407.15725.

[24] Y. Zhang, G. Cao, Z. Kong, *et al.*, *Journal of Semiconductors* **45**, 122102 (2024).

[25] L. A. Terrazos, C. Kloeffel, R. Winkler, and D. Loss, *Physical Review B* **103**, 115201 (2021).

[26] W. J. H. Berghuis, S. Buckley, G. Scappucci, *et al.*, *Journal of Applied Physics* **130**, 135303 (2021).

[27] S. Sioncke, J. Ceuppens, A. Delabie, D. Lin, M. Caymax, *et al.*, *Microelectronic Engineering* **88**, 1553 (2011).

[28] S. Sioncke, J. Ceuppens, S. De Gendt, *et al.*, *Microelectronic Engineering* **88**, 532 (2011).

[29] K. Sardashti, K.-T. Hu, K. Tang, S. Madisetti, P. McIntyre, S. Oktyabrsky, S. Siddiqui, B. Sahu, N. Yoshida, J. Kachian, L. Dong, B. Fruhberger, and A. C. Kummel, *Applied Physics Letters* **108**, 011604 (2016).

[30] M. Ke, S. Ding, A. Guo, *et al.*, *Applied Physics Letters* **109**, 062103 (2016).

[31] H. Wen, X. Chen, H. Li, *et al.*, *AIP Advances* **10**, 025020 (2020).

[32] J. Robertson, *Reports on Progress in Physics* **69**, 327 (2006).

[33] A. Delabie, B. Brijs, M. Caymax, *et al.*, *Journal of Applied Physics* **97**, 064104 (2005).

[34] M. Caymax, B. Brijs, A. Delabie, *et al.*, *Electrochemical and Solid-State Letters* **9**, G96 (2006).

[35] V. A. Chellappan, S. Kumar, and M. K. Hudait, *ECS Journal of Solid State Science and Technology* **3**, N35 (2014).

[36] M. Breedon, S. Wolf, S. T. Ueda, K. Tang, P. McIntyre, and A. C. Kummel, *Applied Surface Science* **478**, 1065 (2019).

[37] M. Eichenfield, J. Chan, R. M. Camacho, K. J. Vahala, and O. Painter, *Nature* **462**, 78 (2009).

[38] Y. Tsaturyan, A. Barg, A. Simonsen, and A. Schliesser, *Nature Nanotechnology* **12**, 776 (2017).

[39] S. Krinner, S. Storz, P. Kurpiers, P. Magnard, J. Heinsoo, R. Keller, J. Luetolf, C. Eichler, and A. Wallraff, *EPJ Quantum Technology* **6**, 2 (2019).

[40] J. M. Elzerman, R. Hanson, L. H. Willems van Beveren, B. Witkamp, L. M. K. Vandersypen, and L. P. Kouwenhoven, *Nature* **430**, 431 (2004).

[41] K. Ono, D. G. Austing, Y. Tokura, and S. Tarucha, *Science* **297**, 1313 (2002).

[42] A. C. Johnson, J. R. Petta, C. M. Marcus, M. P. Hanson, and A. C. Gossard, *Nature* **435**, 925 (2005).

[43] M. Field, C. G. Smith, M. Pepper, D. A. Ritchie, J. E. F. Frost, G. A. C. Jones, and D. G. Hasko, *Phys. Rev. Lett.* **70**, 1311 (1993).

[44] D. J. Reilly, C. M. Marcus, M. P. Hanson, and A. C. Gossard, *Appl. Phys. Lett.* **91**, 162101 (2007).

[45] J. I. Colless, A. C. Mahoney, J. M. Hornibrook, A. C. Doherty, D. J. Reilly, H. Lu, and A. C. Gossard, *Phys. Rev. Lett.* **110**, 046805 (2013).

[46] A. C. Betz, R. Wacquez, M. Vinet, X. Jehl, A. L. Saraiva, M. Sanquer, A. J. Ferguson, and M. F. Gonzalez-Zalba, *Nano Letters* **15**, 4622 (2015).

[47] A. Morello, J. J. Pla, F. A. Zwanenburg, K. W. Chan, H. Huebl, M. Mottonen, C. D. Nugroho, C. Yang, J. van Donkelaar, A. D. C. Alves, D. N. Jamieson, C. C. Escott, L. C. L. Hollenberg, R. G. Clark, and A. S. Dzurak, *Nature* **467**, 687 (2010).

[48] J. R. Petta, A. C. Johnson, J. M. Taylor, E. A. Laird, A. Yacoby, M. D. Lukin, C. M. Marcus, M. P. Hanson, and A. C. Gossard, *Science* **309**, 2180 (2005).

[49] T. Lundberg, D. J. Ibberson, J. Li, L. Hulin, J. C. Abadillo-Uriel, M. Filippone, B. Bertrand, A. Nunnenkamp, and M. F. Gonzalez-Zalba, *npj Quantum Information* **10**, 28 (2024).

[50] J. Yoneda, K. Takeda, T. Otsuka, T. Nakajima, M. R. Delbecq, G. Allison, T. Honda, S. Oda, Y. Hoshi, N. Usami, S. Saito, T. Ito, A. Oiwa, and S. Tarucha, *Nature Nanotechnology* **13**, 102 (2018).

[51] A. West, B. Hensen, B. Undseth, S. Asaad, F. Torres, T. Tanttu, M. A. Fogarty, A. Laucht, F. E. Hudson, K. M. Itoh, M. Veldhorst, and A. S. Dzurak, *Nature Nanotechnology* **14**, 437 (2019).

[52] J. M. Hornibrook, J. I. Colless, A. C. Mahoney, A. Powell, M. Wyn-Jones, J. R. Prance, H. Lu, A. C. Gossard, and D. J. Reilly, *Phys. Rev. Applied* **3**, 024010 (2015).

[53] S. Weinreb, J. C. Bardin, H. Mani, and G. Jones, *IEEE Transactions on Microwave Theory and Techniques* **55**, 2306 (2007).

[54] C. Barthel, M. Kjærgaard, J. Medford, M. Stopa, C. M. Marcus, M. P. Hanson, and A. C. Gossard, *Phys. Rev. B* **81**, 161308 (2010).

[55] A. Lukashenko and A. V. Ustinov, *Review of Scientific Instruments* **79**, 084701 (2008).

[56] H. Bluhm, S. Foletti, I. Neder, M. Rudner, D. Matalu, V. Umansky, and A. Yacoby, *Nature Physics* **7**, 109 (2011).

[57] S. Weinreb, in *2007 USNC/URSI National Radio Science Meeting* (2007) nRAO/Caltech technical report; cryogenic LNA design for 1–2 GHz.

[58] E. W. Bryerton, M. Morgan, and M. W. Pospieszalski, *IEEE Radio Wireless Symp.*, 358 (2013).

[59] B. M. Freeman, J. S. Schoenfield, and H. Jiang, *Applied Physics Letters* **108**, 253108 (2016).

[60] P. Huang and X. Hu, *Physical Review B* **90**, 045301 (2014).

[61] A. V. Khaetskii, D. Loss, and L. Glazman, *Physical Review B* **64**, 125316 (2001).

[62] X. Hu and S. Das Sarma, *Physical Review Letters* **96**, 100501 (2006).

[63] D. M. Zajac, A. J. Sigillito, M. Russ, F. Borjans, J. M. Taylor, G. Burkard, and J. R. Petta, *Science* **359**, 439 (2018).

[64] W. Huang, C. H. Yang, K. W. Chan, T. Tanttu, B. Hensen, R. C. C. Leon, M. A. Fogarty, J. C. C. Hwang, F. E. Hudson, K. M. Itoh, A. Morello, A. Laucht, and A. S. Dzurak, *Nature* **569**, 532 (2019).

[65] X. Mi, M. Benito, S. Putz, D. M. Zajac, J. M. Taylor, G. Burkard, and J. R. Petta, *Nature* **555**, 599 (2018).

[66] A. J. Landig, J. V. Koski, P. Scarlino, C. Reichl, W. Wegscheider, T. Ihn, K. Ensslin, and A. Wallraff, *Nature* **560**, 179 (2018).

[67] L. M. K. Vandersypen, H. Bluhm, J. S. Clarke, A. S. Dzurak, R. Ishihara, A. Morello, D. J. Reilly, L. R. Schreiber, and M. Veldhorst, *npj Quantum Information* **3**, 34 (2017).